A Comparative Study between a Failed and a Successful Eruption Initiated from the Same Polarity Inversion Line in AR 11387

Lijuan Liu[1] , Yuming Wang[2] , Zhenjun Zhou[1] , Karin Dissauer[3] , Manuela Temmer[3] , and Jun Cui[1,4]
[1] School of Atmospheric Sciences, Sun Yat-sen University, Zhuhai, Guangdong, 519082, People's Republic of China; ljliu@mail.ustc.edu.cn
[2] CAS Key Laboratory of Geospace Environment, Department of Geophysics and Planetary Sciences, University of Science and Technology of China, Hefei, Anhui, 230026, People's Republic of China; ymwang@ustc.edu.cn
[3] Institute of Physics, University of Graz, Universitätsplatz 5/II, A-8010 Graz, Austria
[4] CAS Key Laboratory of Lunar and Deep Space Exploration, National Astronomical Observatories, Chinese Academy of Sciences, Beijing, 100012, People's Republic of China

Abstract

In this paper, we analyzed a failed and a successful eruption that initiated from the same polarity inversion line within NOAA AR 11387 on 2011 December 25. They both started from a reconnection between sheared arcades, with distinct pre-eruption conditions and eruption details: before the failed one, the magnetic fields of the core region had a weaker non-potentiality; the external fields had a similar critical height for torus instability, and a similar local torus-stable region, but a larger magnetic flux ratio (of low corona and near-surface region) compared to the successful one. During the failed eruption, a smaller Lorentz force impulse was exerted on the outward ejecta; the ejecta had a much slower rising speed. Factors that might lead to the initiation of the failed eruption are identified: (1) a weaker non-potentiality of the core region, and a smaller Lorentz force impulse gave the ejecta a small momentum; (2) the large flux ratio, and the local torus-stable region in the corona provided strong confinements that made the erupting structure regain an equilibrium state.

Key words: Sun: activity – Sun: coronal mass ejections (CMEs) – Sun: flares – Sun: magnetic fields – Sun: photosphere

Supporting material: animations

1. Introduction

Solar flares and coronal mass ejections (CMEs) are the most energetic phenomena in the solar atmosphere, and are suggested to be different manifestations of the same magnetic explosive process when associated (e.g., Harrison 1995; Lin & Forbes 2000). Their association rate generally increases with the intensities and the durations of the flares. For example, in a survey that covered flares during 1995–2005, association rates of 40%, 60%, and 89% in *GOES* C5.7-, M3.2-, X3-class flares, and 100% in flares of >180 minutes was found (Yashiro et al. 2006). However, exceptions like successive X-class flares without accompanied CMEs do exist (e.g., Wang & Zhang 2007; Sun et al. 2015; Thalmann et al. 2015; Liu et al. 2016a).

Flares accompanied by CMEs are referred to as "eruptive" flares, while those without them are known as "confined" flares. Some confined flares that show signs of ejecta that failed to fully erupt are called "failed/confined eruptions" (e.g., Ji et al. 2003; Alexander et al. 2006). It should be noted that sometimes the observable ejecta may even appear in the inner region of the fields of view (FOVs) of coronagraphs, as literal "CMEs," but these ejecta failed to propagate to a large distance in the corona. These kinds of eruptions may not be magnetically driven, or may at least be different from the flux-rope-related CMEs, therefore they are also defined as failed eruptions (Vourlidas et al. 2010, 2013).

Successful eruptions, i.e., CMEs propagating into interplanetary space, may cause strong geomagnetic disturbances. Hence, it is important for space weather forecasting to successfully identify the difference between explosive phenomena with and without successfully escaped ejecta. Extensive research on the subject of "confined" and "eruptive"

flares, as well "failed/confined" and "successful" eruptions, has been done by, e.g., Török & Kliem (2005), Wang & Zhang (2007), Cheng et al. (2011), and Sun et al. (2015).

In most models, an eruption is usually driven by a core structure in the form of a magnetic flux rope (e.g., Amari et al. 1999, 2000; Roussev et al. 2003; Török & Kliem 2005), irrespective of the formation time (prior to or during the eruption) of the flux rope. The core structure can be tracked if some coupled plasma structures, e.g., sigmoid, filament, prominence, and hot channel, are observable (e.g., Canfield et al. 1999; Zhang et al. 2012; Schmieder et al. 2013). Both theoretical and observational work confirm that helical kink instability is one of the onset mechanisms for eruptions, which occurs when the twist of the magnetic field lines exceeds a critical value (e.g., Török & Kliem 2005; Guo et al. 2010; Kumar et al. 2012); torus instability is another important mechanism for full eruptions, which occurs when the external fields decrease fast enough (e.g., Kliem & Török 2006; Fan 2010). Accordingly, studies on the magnetic conditions in active regions (ARs) mainly focus on two aspects. One is the non-potentiality of the core magnetic fields, such as twist number, electric current, magnetic free energy, and magnetic helicity, etc. (e.g., Falconer et al. 2002, 2006; Nindos & Andrews 2004; Sun et al. 2015). The other is the confinement of the external magnetic fields, measured by the decay of the magnetic fields with increasing height, i.e., decay index (Török & Kliem 2005), or a ratio of magnetic fluxes at different heights (Wang & Zhang 2007). Confined events usually have a weaker non-potentiality in the core region (e.g., Sun et al. 2015; Liu et al. 2016a), and a stronger confinement in the low corona than successful eruptions (e.g., Liu 2008). Additionally, an eruption position close to the center of the AR (Wang &

Zhang 2007; Cheng et al. 2011; Chen et al. 2015), a lack of opened or opening overlying magnetic fields (Ji et al. 2003), or an asymmetry of the magnetic backgrounds (Liu et al. 2009), may play roles in confining the eruptions.

The topology of the magnetic fields that is involved in the eruption, including that of the core fields and the overlying fields, will determine the eruption details. Therefore, a similar magnetic environment tends to produce similar eruptions. For example, homologous CMEs/flares, with similar eruptiveness, can occur from the same region within an AR, e.g., from the same polarity inversion line (PIL; Zhang & Wang 2002; DeVore & Antiochos 2008; Chandra et al. 2011; Wang et al. 2013; Liu et al. 2017; Vemareddy 2017). PILs are the boundaries of adjacent flux concentrations with inversed polarities. The core structures of the eruptions, i.e., flux ropes or sheared arcades, usually reside above the PILs. The same source PIL naturally hints at a similar magnetic environment, but sometimes does not guarantee activities with similar eruptiveness. For example, Shen et al. (2011) studied a series of filament eruptions from the same source region, of which only one eruption successfully escaped the Sun. They found that the field strength at the low corona, the decay index, and the asymmetry properties of the extrapolated overlying fields for the failed and successful eruptions had no significant differences, and argued that besides the confinement, the energy released in the low corona may also be crucial for an eruption to fully erupt. Hence, further comparative studies are needed.

In this paper, from the view of failed/successful eruptions, we present a comparative study between two eruptions that initiated from the same PIL within NOAA AR 11387. The first one was a failed eruption associated with a C8.4-class *GOES* soft X-ray (SXR) flare (2011-12-25T11:20 UT); the second one was a successful eruption that escaped the Sun and evolved into a CME, associated with a M4.0-class flare (2011-12-25T18:11 UT). We hereafter refer to the first, i.e., the failed (second, successful) one and its corresponding flare as eruption1 and flare1 (eruption2 and flare2). By performing a combined analysis, including eruption details and the evolution of the magnetic conditions based on stereoscopic observations, we try to discover a physical explanation for events that initiated from a possibly similar magnetic environment but with different eruptiveness. The paper is organized as follows. Data and methods are introduced in Section 2. Results are presented in Section 3. A summary and discussion are given in Section 4.

2. Data and Methods

The two eruptions both occurred near the coordinates S20W20 (see Table 1 for details), and are well observed by *SDO* (*Solar Dynamics Observatory*, Pesnell et al. 2012). *STEREO-A* (*Solar TErrestrial RElations Observatory-Ahead*, Kaiser et al. 2008) had a separation angle of 107° from *SDO*, giving an additional limb-view for the eruptions. We study the on-disk flaring evolution, using *SDO*/AIA (Atmospheric Imaging Assembly, Lemen et al. 2012) data. *SDO*/AIA observes in seven EUV passbands and three UV passbands with a cadence up to 12 s and and a resolution of 0.6 arcsecs. We analyze the rising motion of the eruptions, using data from the EUVI (Extreme Ultraviolet Imager, Wuelser et al. 2004), and COR1 and COR2 (Inner and Outer Coronagraphs, Thompson et al. 2003), which are all contained in SECCHI (Sun Earth Connection Coronal and Heliospheric Investigation,

Howard et al. 2008) on board *STEREO-A*. We further apply a CME detection tool (Bein et al. 2011, 2012) to track the eruption structure in EUVI, COR1, and COR2 images, by which its kinematics is obtained using a spline fit method.

In addition to the above data sets, photospheric vector magnetograms from *SDO*/HMI (Helioseismic and Magnetic Imager, Hoeksema et al. 2014) are used to analyze the eruption-related magnetic conditions. We take a subset of SHARPs (Space-weather HMI Active Region Patches, Bobra et al. 2014) data products that automatically track an AR (or AR clusters). SHARPs are remapped from CCD coordinates into heliographic coordinates with cylindrical equal area (CEA), with a resolution of 0.36 Mm per pixel and a time cadence of 720 s. Using SHARP data, we are able to calculate photospheric parameters, e.g., magnetic flux Φ, shear angle S, current density J_z, current helicity h_c, energy density ρ, etc., in the whole AR or in a sub-region within the AR (cf. the detailed calculation formulas in Table 1).

Using the DAVE4VM (Differential Affine Velocity Estimator for Vector Magnetograms, Schuck 2008) method for a time-series of SHARP vector magnetograms, we can find the photospheric plasma velocity ($\mathbf{V}$). By subtracting the field-aligned plasma flow, $(\mathbf{V} \cdot \mathbf{B})\mathbf{B}/B^2$, from $\mathbf{V}$, the velocity perpendicular to the magnetic fields, denoted by $\mathbf{V}_\perp$, can be obtained. Accordingly, the relative magnetic helicity flux through the photosphere can be calculated by

$$\left. \frac{dH}{dt} \right|_S = 2 \int_S (\mathbf{A}_p \cdot \mathbf{B}_t) V_{\perp n} dS - 2 \int_S (\mathbf{A}_p \cdot \mathbf{V}_{\perp t}) B_n dS, \quad (1)$$

where $\mathbf{A}_p$ refers to the vector potential of the potential magnetic fields that have the same vertical component as the photospheric vector magnetic fields, B_t (B_n) refers to the tangential (vertical) component of the fields, and $V_{\perp t}$ ($V_{\perp n}$) refers to the tangential (vertical) component of $\mathbf{V}_\perp$. The left term of the above equation denotes the helicity injection rate contributed by the emergence of the twisted flux tube, while the right term refers to the helicity injection rate due to the shear motion on the photosphere (e.g., Berger 1984; Liu & Schuck 2012; Liu et al. 2014).

No direct observation of coronal magnetic fields is available. Thus, the three-dimensional (3D) coronal magnetic fields are reconstructed by nonlinear force-free fields (NLFFF; Wiegelmann 2004; Wiegelmann et al. 2006, 2012) and a potential fields (PF) extrapolation method (e.g., Sakurai 1989), using the photospheric vector magnetograms as boundaries. Magnetic free energy can therefore be calculated by subtracting the magnetic potential energy from the total magnetic energy, i.e., with

$$E_F = E_N - E_P = \int_V \frac{B_N^2}{8\pi} dV - \int_V \frac{B_P^2}{8\pi} dV, \quad (2)$$

in which B_N refers to the NLFFFs and B_P refers to the PFs, and dV denotes the elementary volume. The decay index that measures the decrease of the external magnetic fields with increasing height can be calculated by

$$n = -\frac{\partial \ln B_{\rm ex}(h)}{\partial \ln h}, \quad (3)$$

where h refers to the height, and $B_{\rm ex}$ is the horizontal component of the external potential magnetic fields, since PFs play a major role in confining the eruption in torus

Table 1
Characteristics of the Two Eruptions

			Event1	Event2	Unit
Flare	Begin		2011-12-25T11:20 UT	2011-12-25T18:11 UT	
	Peak		11:26	18:16	
	End		11:31	18:20	
	Duration		11	9	minutes
	Location		S23W22	S22W26	
Eruption[a]			Confined	Eruptive	
	Core	H_h	0.24	...	R_{Sun}
		V_{peak}	178.2	...	km s^{-1}
	CME	H_h	...	>13	R_{Sun}
		V_{peak}	...	1041.4	km s^{-1}
Parameters[b]	FPIL	Φ	2.71	8.17	$10^{20} Mx$
		Area	92.75	185.76	Mm^2
		$\overline{B}$	479 ± 13	814 ± 10	G
		$\overline{S}$	50.88 ± 0.03	56.80 ± 0.02	Degree
		$\overline{J_z}$	0.61 ± 0.02	−1.86 ± 0.02	mA m^{-2}
		$\overline{h_c}$	0.05 ± 0.00	0.13 ± 0.00	G^2 m^{-1}
		$\overline{\rho}$	1.61 ± 0.00	4.31 ± 0.00	10^{19} erg cm^{-3}
	Corona	Critical height	13.11 ± 0.73	10.12 ± 0.73	Mm
		$\Phi(42)/\Phi(2)$	0.08	0.04	
		E_f	2.27 ± 0.45	4.71 ± 0.94	$\times 10^{31}$ erg
Change		ΔB_h	+124	+160	G
		ΔE_f	−0.47	−0.83	10^{31} erg
		ΔF_z	+0.11	+1.63	$10^{22} dyn$

Notes.
[a] H_h represents the highest height the eruption structure reached; V_{peak} represents the peak velocity of the eruption. "..." means no result is obtained.
[b] Unsigned magnetic flux $\Phi(h)$ is calculated by $\sum |B_z(h)| dA$ in the plane intersected by the FPIL mask; h refers to an arbitrary height. Mean shear angle $\overline{S}$ is computed from $\frac{1}{N}\sum arccos\left(\frac{B_o \cdot B_p}{|B_o||B_p|}\right)$, where $B_o (B_p)$ denotes the observed (potential) fields. Mean current density J_z is calculated by $\frac{1}{N}\sum\left(\frac{\partial B_y}{\partial x} - \frac{\partial B_x}{\partial y}\right)$. Mean current helicity $\overline{h_c}$ is calculated by $\frac{1}{N}\sum\left| B_z\left(\frac{\partial B_y}{\partial x} - \frac{\partial B_x}{\partial y}\right)\right|$. Mean free energy density $\overline{\rho}$ is calculated by $\frac{1}{N}\sum\frac{1}{8\pi}(B_o^2 - B_p^2)$. All formulas described above are adapted from Table 3 in Bobra et al. (2014).

instability theory (Török & Kliem 2005). A ratio of the unsigned magnetic fluxes in the low corona ($h \approx 42$ Mm) and in the near-surface region ($h \approx 2$ Mm), which additionally measures the confinement of the overlying fields to the core region (Wang & Zhang 2007; Sun et al. 2015), can be calculated by $\Phi(42)/\Phi(2)$. 42 Mm is found to be a typical height for eruption onset (Liu 2008). $\Phi(h)$ is calculated by $\sum |B_z(h)| dA$ in a plane with a height of h Mm, where B_z refers to the vertical component of the magnetic fields and dA refers to the elementary area of the plane.

To study the magnetic parameters in the region that is most largely involved in the flare, a "flaring PIL" (FPIL) is obtained following the method described in Sun et al. (2015): the PIL pixels are first located in a B_z map, and then dilated with a circular kernel ($r \approx 3$ Mm); the flaring pixels are first located in an AIA 1600 Å map near the peak time of the flare, with a threshold of $A_m + 3 \times A_d$, where A_m and A_d are the mean value and the standard deviation of the 1600 Å image, and then dilated with a large kernel; finally, the FPIL is determined as the intersection between the dilated PIL pixels and the flaring pixels. Within the region, the parameters in Table 1 are calculated. Additionally, the change of the vertical Lorentz

force during the eruption, whose temporal integral can represent the force impulse that provides the outward ejecta's momentum, is calculated by:

$$\delta F_{z,\mathrm{upward}} = \frac{1}{8\pi} \int dA(\delta B_h^2 - \delta B_z^2), \qquad (4)$$

where B_z (B_h) refers to the vertical (horizontal) component of the magnetic fields, and dA refers to the elementary area (Fisher et al. 2012; Petrie 2012, 2013; Wang & Liu 2015).

With the data and methods introduced above, we perform the analyses.

3. Results

Figure 1 displays the magnetic source region and the accompanying flares of the two eruptions. The source AR had a multipolar configuration (as seen in Figure 1(a)). Both eruptions were initiated from the same PIL (yellow line in Figure 1(a)), which was formed by two closely placed flux concentrations with opposite polarities (enclosed in white boxes in Figures 1(a), (c), (e)). The two flares had different magnitudes, C8.4-class for flare1 and M4.0-class for flare2, respectively (Figures 1(b), (d)), but almost the same durations (9 and 11 minutes). See more
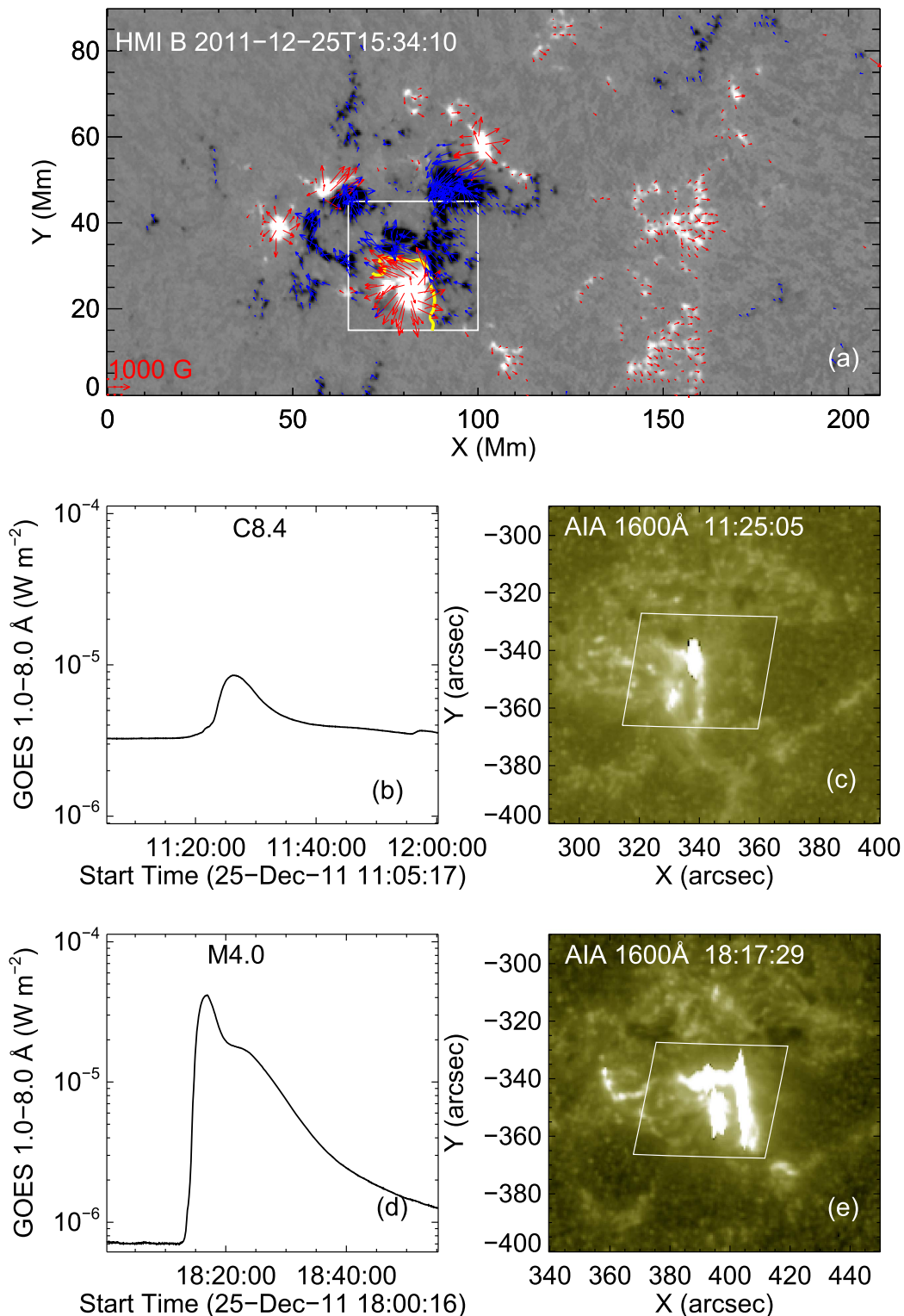
Figure 1. Overview of the magnetic source and the associated flares. (a) Vector magnetic fields of NOAA AR 11387 at a time instance between the two eruptions in the CEA heliographic coordinates; the vertical components of the vector magnetic fields (B_z) are plotted as background, and the white/black patches refer to the positive/negative B_z that saturate at ±800 Gausses; the red/blue arrows refer to the horizontal component of the vector magnetic fields (B_h) that originate from the positive/negative polarities; the yellow line outlines the PIL that the two eruptions originated from; the white box encloses the flux concentrations that form the PIL. (b) and (d) are the GOES SXR curves of the two flares, (b) for flare1 and (d) for flare2. (c) and (e) are the corresponding observations in AIA/1600 Å near the flare peaks, showing the flare ribbons along the PIL, (c) for flare1 and (e) for flare2. The white rectangles in (c) and (e) are the white box in (a) but remapped to the CCD coordinates.

flaring details in Table 1. They all produced flare ribbons along the source PIL (as seen in Figures 1(c), (e)). For each eruption, we analyze their eruption details, pre-eruption magnetic conditions, and eruption-related changes.

3.1. Eruption Details

Figure 2 shows the eruption process of the failed eruption (eruption1) observed by AIA (panels (a)–(d)), EUVI
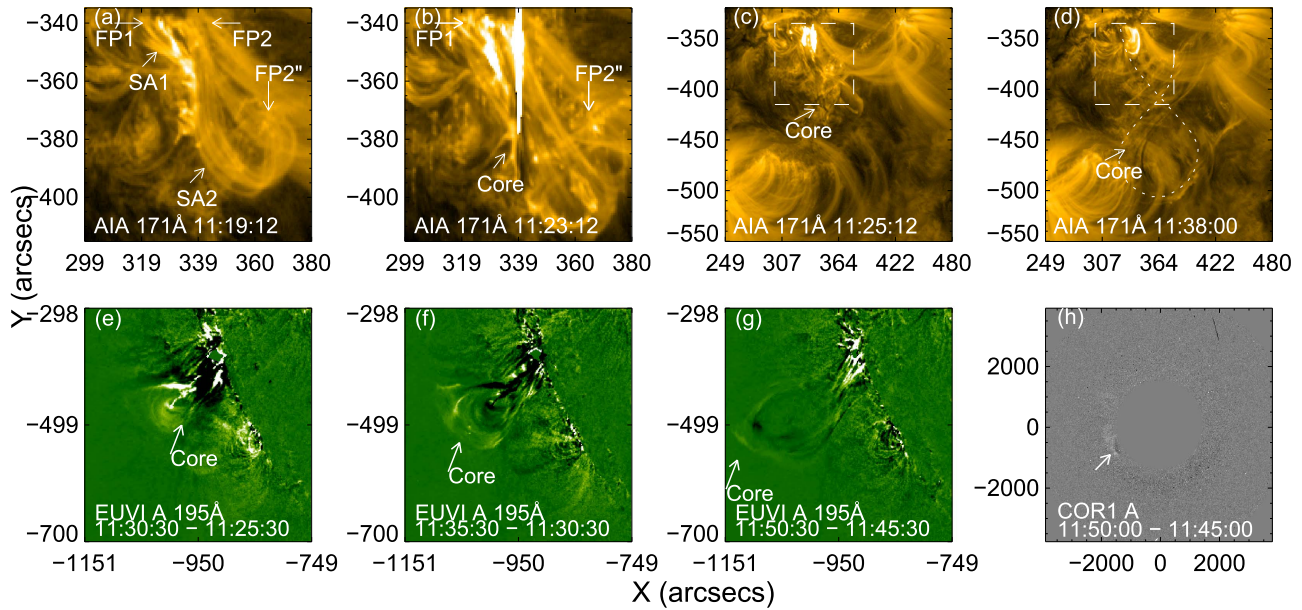
Figure 2. Snapshots for the failed eruption. (a)–(d) Flaring and eruption observed by AIA/171 Å. (e)–(g) Eruption of the core structure observed by EUVI A 195 Å from a limb-view. (h) Faint coronal outflow observed in COR1 A. Arrows SA1 and SA2 in (a) mark the two sets of sheared arcades involved in the eruption. Their footpoints are marked as FP1 (for SA1, short for footpoint1), FP2 and FP2″ (for SA2) in (a) and (b), respectively. The arrows labeled "Core" in (b)–(g) refer to the structure formed during the flare that drove the eruption but failed to erupt out. The white dotted line in (d) outlines the γ shape of the core structure during the eruption. Panels (c) and (d) have the same on-disk FOV, which is different from the FOV of (a) and (b). The FOV of (a) and (b) is outlined by the white boxes in (c) and (d) for comparison. The online animation lasts from 11:05 to 12:15, covering the eruption details not only shown above but also observed in AIA/131, 94, 304, 1600 Å, plus the GOES soft X-ray curve and evolution of the radial component (B_r) of the photospheric magnetic fields observed by HMI.

(An animation of this figure is available.)

A (panels (e)–(g)), and COR1 A (panel (h)). Before the onset of the flare, two sets of sheared arcades (marked by arrows SA1 and SA2 in Figure 2(a)) were discernible in multiple wavelengths. The two sets of sheared arcades both lie above the source PIL. See more supporting evidence from the extrapolated magnetic fields in Section 3.3. The locations of the northern footpoints of the two sets of arcades (marked by FP1 and FP2 in Figure 2) were very close. Flaring between the two sets of sheared arcades can be observed. After the onset of the flare, mixture and exchange between the northern footpoints of SA1 and SA2 can be identified (see Figure 2(b)). A structure connecting the northern footpoint of SA1 (FP1 in Figures 2(a) and (b)) and the southern footpoint of SA2 (FP2″ in Figures 2(a) and (b)) formed and acted as the core structure of the eruption (see Figures 2(c) and (d)). The structure showed a clear writhing motion, which converted the twist of the plasma-coupled field lines into the writhe of the axis of the flux-rope-like core structure, then grew into a γ shape in AIA observation (outlined by the white dotted line in Figure 2(d)), faded gradually, and finally became invisible. Accompanying plasma drainage downward toward the solar disk can be observed. For more details see the online animation. The core structure showed an upward motion, as observed by EUVI A with a limb-view (Figures 2(e)–(g)), and finally halted at around 0.24 R_{Sun} and gradually became invisible. Meanwhile, extremely faint outflow can be observed in the inner boundary of the FOV of COR1 A (Figure 2(h)), which soon decelerated and diffused, following the motion of the failed erupted core structure. In conclusion, this cannot be defined as a successful CME as defined in Section 1.

The kinematical evolution of the core structure is shown in Figure 3 (red curve), and was obtained by the CME detection tool introduced in Section 2. The core structure was first

observed by EUVI A 195 Å at a height of $\sim 0.01 R_{\text{Sun}}$ above the solar surface, then slowly rose and stopped at the highest position around 0.24 R_{Sun}. Accordingly, the velocity of the core structure peaked at the core's first appearance, then decreased gradually to 0. The inner corona outflow that appeared in COR1 A was extremely faint and diffuse, without a coherent shape or clear front, leading to a large uncertainty in its detection. Thus, its kinematics is not obtained.

In summary, the failed eruption was driven by a flux-rope-like structure that could have formed during the flare. The core structure rose slowly and finally halted/disappeared at around 0.24 R_{Sun}.

Figure 4 shows the eruption process of the successful eruption (eruption2) observed by AIA (panels (a)–(d)), EUVI A (panels (e)–(f)), COR1 A (panel (g)), and COR2 A (panel (h)). Before the onset of the flare, a sigmoid structure can be observed in multiple wavelengths of AIA, which is shown in 94 Å here (Figure 4(a)). Two sets of sheared arcades (marked by SA1 and SA2 in Figure 4(a)) can be identified. See more supporting evidence from the extrapolated magnetic fields in Section 3.3. The corresponding footpoints of the two sets of the sheared arcades (FP1 and FP1″ for SA1, FP2 and FP2″ for SA2 in Figure 4(b)) brightened after the flare onset. The intensity of the flaring kept increasing (Figure 4(c)); the sheared arcades or any structure that formed during the eruption cannot be identified later. After the eruption, post-eruption loops can be observed (Figure 4(d)). See more details in the online animation.

The kinematics of the CME in eruption2 is also checked and shown in Figure 3 (in blue). The CME was first captured by EUVI A at a height around 0.1 R_{Sun}, with a peak velocity of 1041 km s^{-1}, and then expanded quickly and entered the FOV of COR1 A before the flare ended. The velocity of the CME
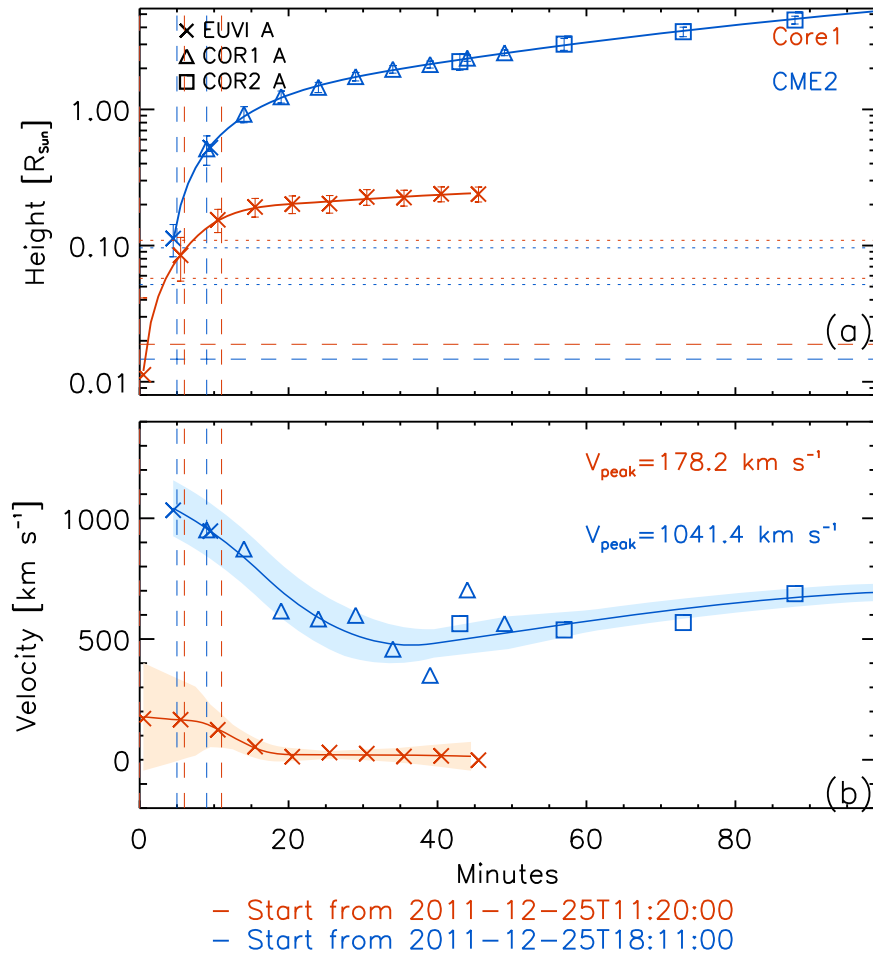
Figure 3. Kinematics of the two eruptions: (a) shows the heights of the eruptions and (b) shows the velocities of the eruptions. The time axes all start from the instances of the flare onsets. The colored vertical dashed lines mark the peak and end times of the flares. The horizontal long dashed lines in (a) mark the critical heights, and the upper two sets of horizontal short dashed lines mark the local torus-stable regions for each eruption (see details in Section 3.2). The X marks are data points measured from observations of EUVI A, the triangle symbols are for COR1 A and the squares are for COR2 A. The height/velocity curves are fitted by a spline fit method to the observed data points. The red curves, points, and text provide information on the core structure of eruption1 (Core1); the blue ones provide information on the CME in eruption2 (CME2). The uncertainties for the height measurements are overplotted as error bars in (a), and those for the velocities are displayed as the colored, shaded regions in (b).

decreased as it propagated, and finally kept at a constant speed around $500\ km\ s^{-1}$.

In summary, the successful eruption released a CME rapidly. There may also be a reconnection between the two sets of sheared arcades during the eruption, similar to the process in the failed eruption, that needs further study based on coronal magnetic field reconstruction (see Section 3.3).

3.2. Pre-eruption Condition

3.2.1. Long-duration Evolution of the AR

In this section, we check the evolution of the source AR, NOAA AR 11387, six hours before each eruption. Figure 5 displays snapshots of the evolving photospheric vector magnetic fields (Figures 5(a)–(c) for eruption1, (e)–(g) for eruption2) and six-hour-averaged velocities $V_\perp$ (Figure 5(d) for eruption1, (h) for eruption2). Before both eruptions, clear magnetic flux emergence can be observed in the B_z magnetograms. For eruption1, the AR already had a multipolar configuration six hours before its onset (Figure 5(a)). The source polarity pairs are highlighted in Figure 5 (white boxes and insets.) Within the region, the positive polarity (white patch) appeared and grew quickly during the six hours, accompanied by a westward

movement that can be distinguished from its displacement. Meanwhile, the negative polarity (black patch) underwent a significant morphological change. The polarity pairs were approaching each other. The B_h component of the magnetic fields (red and blue arrows in Figures 5(a), (b), and (c)) grew with the emergence of the polarities. The tangential components ($V_{\perp t}$, orange arrows in Figure 5(d)) of the six-hour-averaged velocities clearly indicate westward motion, while the vertical velocities ($V_{\perp n}$, cyan contours in Figure 5(d)) indicate significant upflow at the east boundary of the positive polarity. The positive polarity moved westward faster than the negative one, indicating a net converging motion toward the PIL (yellow lines in Figures 5(c) and (d); see online animation).

Before eruption2, flux emergence, especially for the positive flux, still existed in the source polarity pairs (Figures 5(e)–(g)). Shortly before eruption2 (Figure 5(g)), the polarities were much closer to each other than the ones at the time instance before eruption1 (Figure 5(c)), and B_h ran more parallel to the PIL. The six-hour-averaged tangential velocities also indicate a westward movement (orange arrows in Figure 5(h)), while the vertical velocities (cyan contours in Figure 5(h)) indicate a large extent upflow at the east boundary of the positive polarity, which was smaller compared to the upflow before eruption1 (Figure 5(d)).
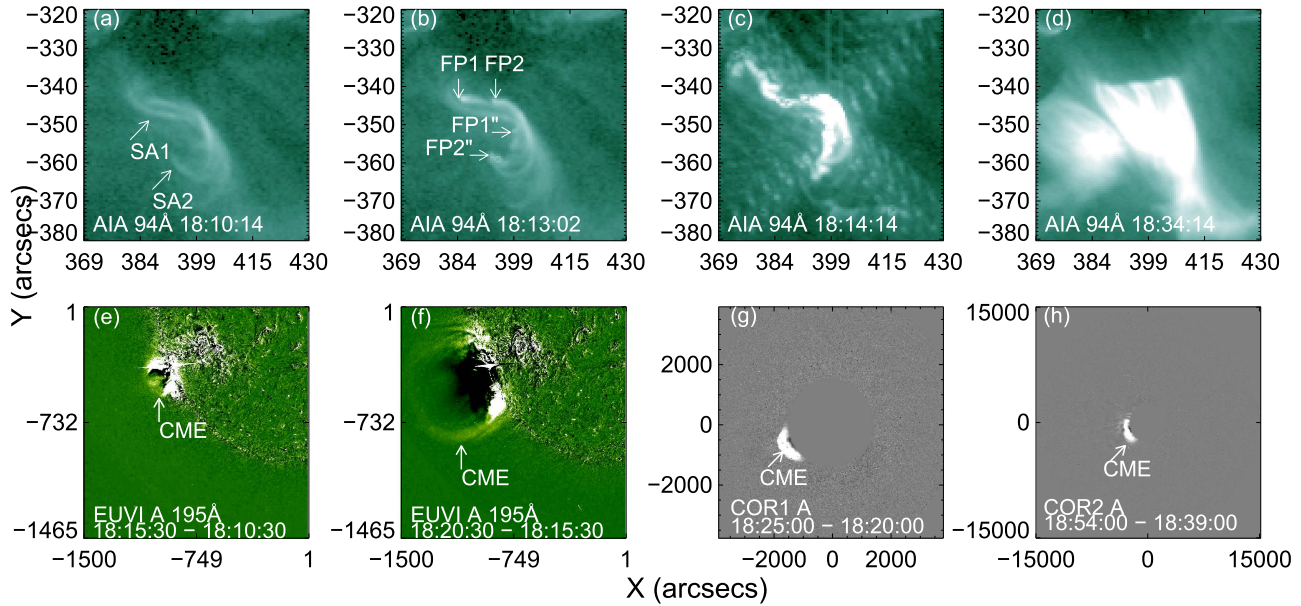
Figure 4. Snapshots of the successful eruption. The layout is similar to that of Figure 2. (a)–(d) are the eruption process observed in AIA/94 Å. Arrows SA1 and SA2 have similar meanings as the ones in Figure 2(a). Their corresponding footpoints are marked by arrows FP1, FP1'' and FP2, FP2''. The former pair is for SA1 and the latter pair is for SA2. (e)–(f) CME observed by EUVI A. (g)–(h) CME observed by COR1 A and COR2 A. The online animation lasts from 18:05 to 18:50, showing the eruption details using a similar layout as the animation corresponding to Figure 2.

(An animation of this figure is available.)

The positive polarity had a faster westward movement and brought the two polarities closer. See the online animation for the evolution of the photospheric vector magnetic fields of the AR.

The temporal evolutions of some key parameters that characterize the properties of the entire AR are displayed in Figure 6. The total, positive, and negative magnetic fluxes (black, orange, cyan curves in Figure 6(a)) increased with time, confirming the flux emergence as observed in the magnetogram snapshots (Figure 5). The flux change rate (dotted black curve in Figure 6(a)) evolved, showing a larger value around 5×10^{20} Mx hr^{-1} before flare1 than the value around 4.2×10^{20} Mx hr^{-1} before flare2. The helicity flux, i.e., the helicity injection rate calculated from Equation (1), including the total, the emergence term, and the shear term are shown in Figure 6(b). The shear term (cyan curve in Figure 6(b)) played a dominant role for the helicity injection. Before eruption1, the shear term had a mean value of $0.69 \pm 0.11 \times 10^{37}$ Mx^2 s^{-1}, while the emergence term had a mean value of $0.43 \pm 0.07 \times 10^{37}$ Mx^2 s^{-1}. Before eruption2, the shear term had a sudden increase after 14:00 UT but decreased again after 17:00 UT, with a peak value reaching 1.48×10^{37} Mx^2 s^{-1}. Meanwhile, the emergence term had a mean value of $0.50 \pm 0.12 \times 10^{37}$ Mx^2 s^{-1} before 16:00 UT, comparable to the mean value before eruption1, and then showed a decreasing trend. Free magnetic energy is also calculated with Equation (2) based on the reconstructed coronal magnetic fields; this calculation is shown in Figure 6(c). The magnetic free energy increased before both eruptions. More free energy was accumulated during the six hours before eruption2 (2.35×10^{31} erg) than the six hours before eruption1 (1.40×10^{31} erg).

In summary, flux emergence, helicity injection, and free energy accumulation existed in the AR before both eruptions. The latter two accumulated more remarkably before the successful eruption.

3.2.2. Magnetic Conditions Prior to the Eruption Onsets

The magnetograms have a time cadence of 12 minutes. To explore the static, pre-eruption magnetic conditions, we choose the ones nearest and prior to the flare onsets, resulting in magnetograms with 10 minutes before flare1, and with 1 minute before flare2. On the photosphere, an FPIL mask (outlined by dotted green lines in Figures 7(a) and (c)), a region that involves the source PIL and the flaring area, is obtained based on the combination of the magnetograms and the images in AIA/1600 Å for each eruption (see the method details in Section 2). We refer to FPIL1 (FPIL2) as the mask for eruption1 (eruption2). The parameters in the FPIL masks are calculated and shown in Table 1. In general, FPIL2 had a larger size than FPIL1, with an unsigned magnetic flux (Φ) of 8.17×10^{20} Mx, which was three times larger than that for FPIL1 (2.71×10^{20} Mx). The mean value of the strength of the magnetic fields ($\bar{B}$) in FPIL2 (814 G), which should not be affected by the mask size, was also larger than that in FPIL1 (479 G). The parameters that measure the non-potentiality of the region all had larger values in FPIL2 than in FPIL1. See details in Table 1 (also covering parameters that measure the confinement of the external potential fields). The two events had similar critical heights (the heights where n reaches the critical value, 1.5, for torus instability) below 15 Mm. The ratio of magnetic fluxes between 42 Mm and 2 Mm for eruption2 (0.04) was lower than that for eruption1 (0.08). The free energy for eruption2 in the total computing volume (4.71×10^{31} erg) was larger than that for eruption1 (2.27×10^{31} erg).

For clarification, Figure 7 displays the pre-eruption free energy map (Figures 7(a) and (c)) of the core region and the distribution of B_h and decay index above the FPIL (Figures 7(b) and (d)). The free energy is integrated from the photosphere to 42 Mm. For both eruptions, the free energy had clear concentrations that covered the majority of the FPIL. The intensity and the size of the free energy concentration for eruption2 were
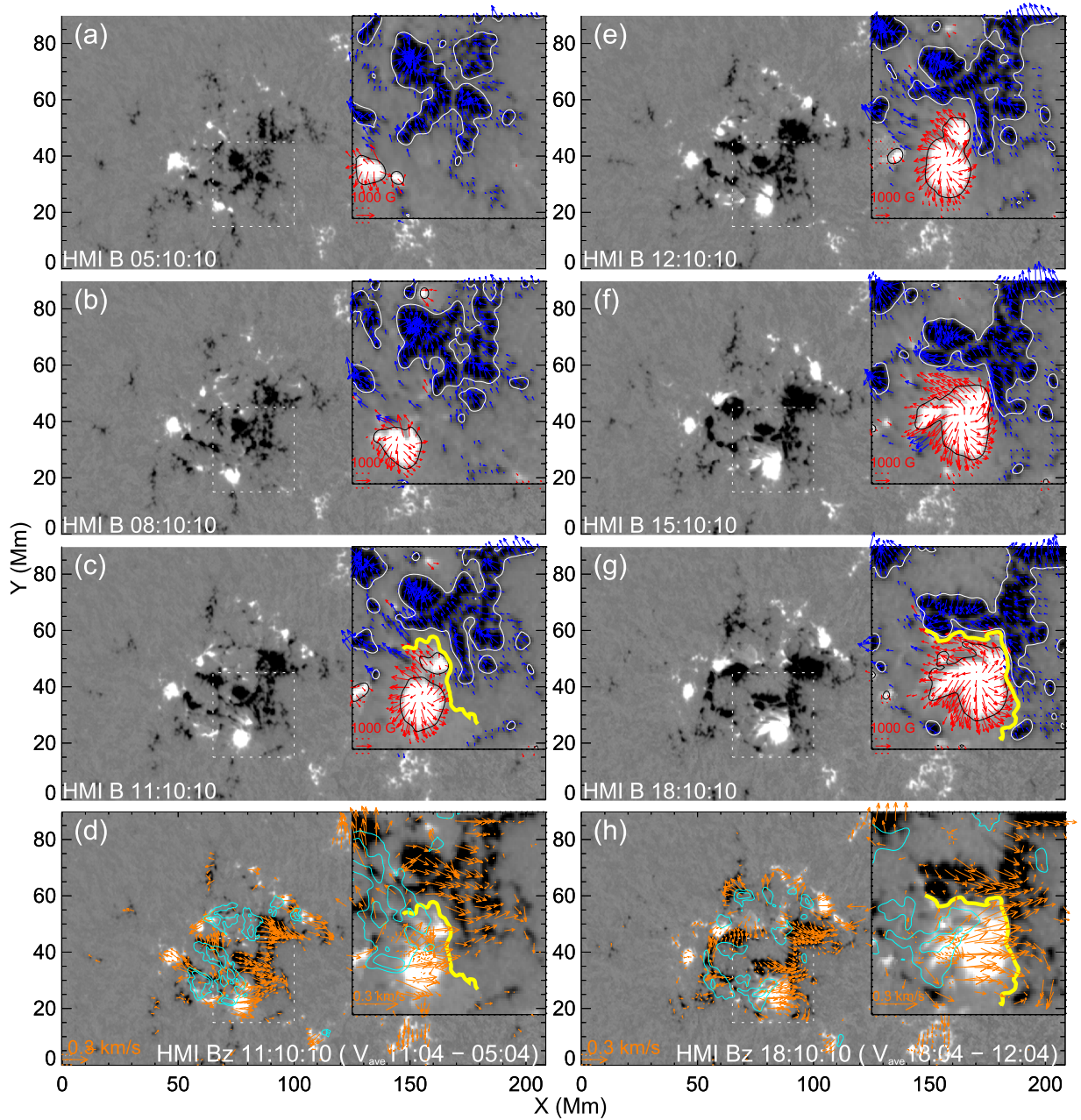
Figure 5. Evolution of the photospheric vector magnetic fields, and the velocities, of the AR six hours before each eruption. (a)–(d) Evolution before eruption1. (e)–(f) Evolution before eruption2. (a)–(c) Maps of B_z before eruption1 every three hours. The white dotted boxes have the same FOV as the white box in Figure 1(a), enclosing the source magnetic polarity pairs, and are enlarged and displayed as insets, with B_h overplotted. The black (white) contours in the insets outline the boundaries of the positive (negative) polarity at 300 (−300) G for clarity. The colored backgrounds and arrows have the same meaning as the ones in Figure 1(a). (d) shows the B_z magnetogram (same as in panel (c)) shortly before the flare, with the six-hour-averaged $V_\perp$ calculated by DAVE4VM overplotted. The orange arrows display the horizontal component of $V_\perp$, while the cyan contours outline the vertical component of $V_\perp$ at [0.05, 0.09] km s^{-1}. The yellow lines in (c) and (d) mark the PIL before eruption1. (e)–(h) have the same layouts as (a)–(d) but for eruption2. The online animation shows the 12 hr evolution of the photospheric vector magnetic fields.

(An animation of this figure is available.)

larger than those for eruption1. Meanwhile, the distributions of the decay index above the FPIL (orange curves in Figures 7(b), (d)) showed the similar variation trend of a "saddle-like" profile: for eruption1, n reached the critical value of 1.5 at around 13.1 Mm, kept increasing, and peaked at around 27 Mm with a value of 2, then decreased and dropped in a local torus-stable region within [40, 76] Mm, and afterward kept increasing with values larger than 1.5; for eruption2, a similar variation trend was found, but with slightly lower heights. n reached the critical

height at around 10.2 Mm, peaked at 21 Mm, and fell into the local torus-stable region within heights of [36, 67] Mm. For the median value of B_h above the FPIL (black curves in Figures 7(b), (d)), the two distributions had a similar variation trends, except with larger values near the photosphere for eruption2.

For each eruption, the pre-eruption critical height (long dashed horizontal line in Figure 3(a)) and torus-stable region (enclosed in the upper two short dashed horizontal lines in Figure 3(a)) are
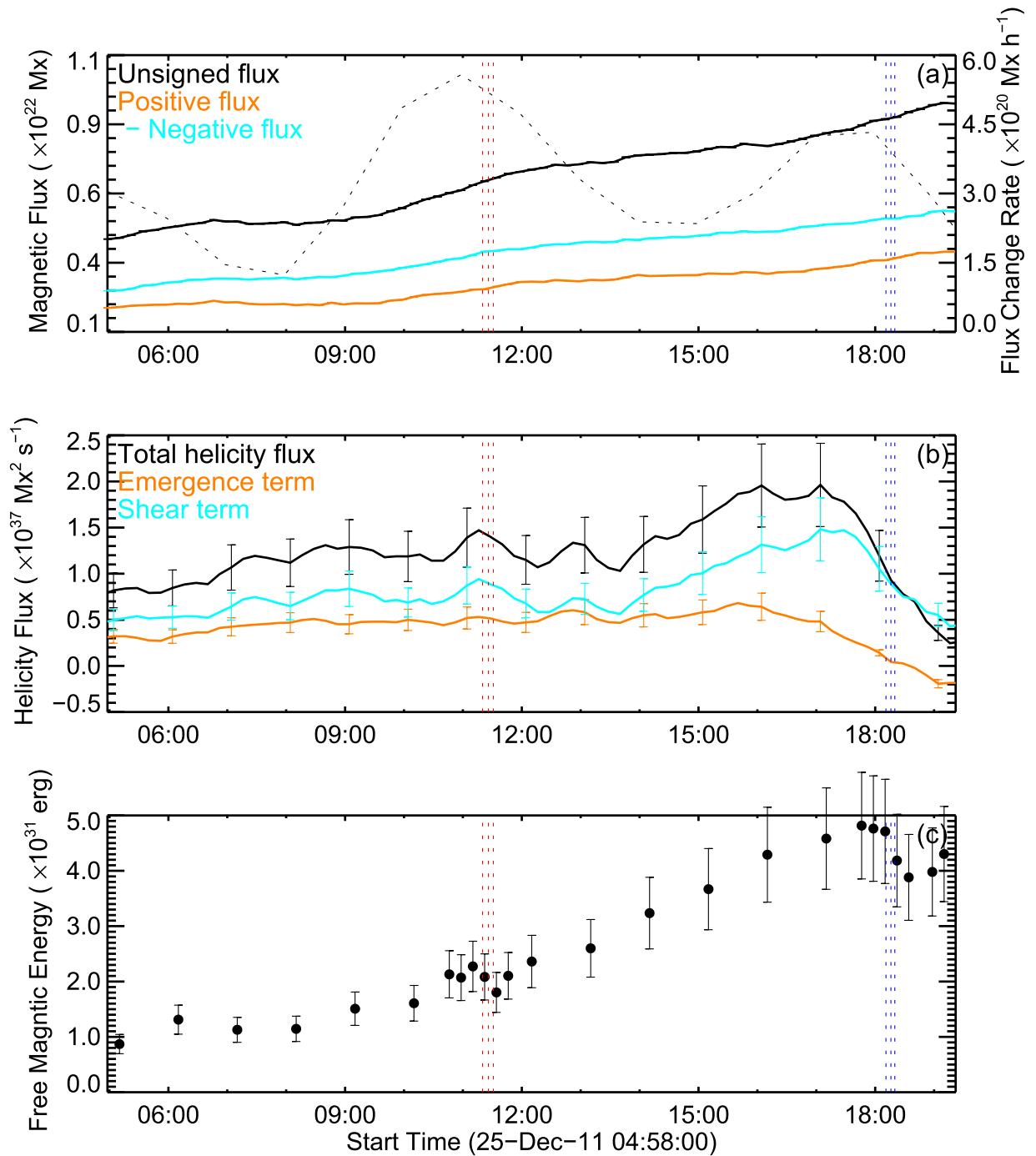
Figure 6. Evolution of magnetic flux, helicity injection rate, and free magnetic energy of the AR, covering the durations of six hours before eruption1 and six hours before eruption2. (a) Evolution of magnetic fluxes: the black solid line is for the total unsigned magnetic flux, the black dotted line is for the magnetic flux change rate, the orange line is for the positive magnetic flux, and the cyan line is for the absolute value of the negative magnetic flux, which is suited for a direct comparison. The uncertainties of the magnetic flux calculated from the error data segment from HMI are overplotted on the curves, which are too small to be distinguished. (b) One-hour-averaged helicity flux calculated by Equation (1): the black line is for the total helicity flux, the orange line is for the helicity flux from the emergence term, and the cyan line is for the helicity flux from the shear term. An uncertainty of 23% of the helicity flux value (a value from Liu & Schuck 2012) is overplotted every 5 data points. (c) Free magnetic energy calculated in the reconstructed magnetic fields by Equation (2). Uncertainties of 20% of the free energy values are overplotted (Thalmann et al. 2008). The energy data points have a cadence of 720 s during the eruption, and 1 hr during other durations. In all panels, the red dotted lines mark the beginning, peaking, and ending times of flare1. The blue dotted lines give the same information, but for flare2.

marked in Figure 3 for comparison. The core structure of the failed eruption had an initial height of $\sim 0.01\,R_{\mathrm{Sun}}$ ($\approx 7\,\mathrm{Mm}$). It rose rapidly in the lower torus-unstable region, and slowed down to a large extent after it passed the torus-stable region. The CME in the successful eruption rose much faster than the failed one, and passed the torus-stable region more quickly.

In summary, before the eruption onset, the core region of the successful eruption displayed a larger non-potentiality than the failed one. Their decay index distributions had a similar variation trend like a "saddle," in which a local torus-stable region was enclosed by two torus-unstable regions. The torus-stable region may play a role in confining the failed eruption.
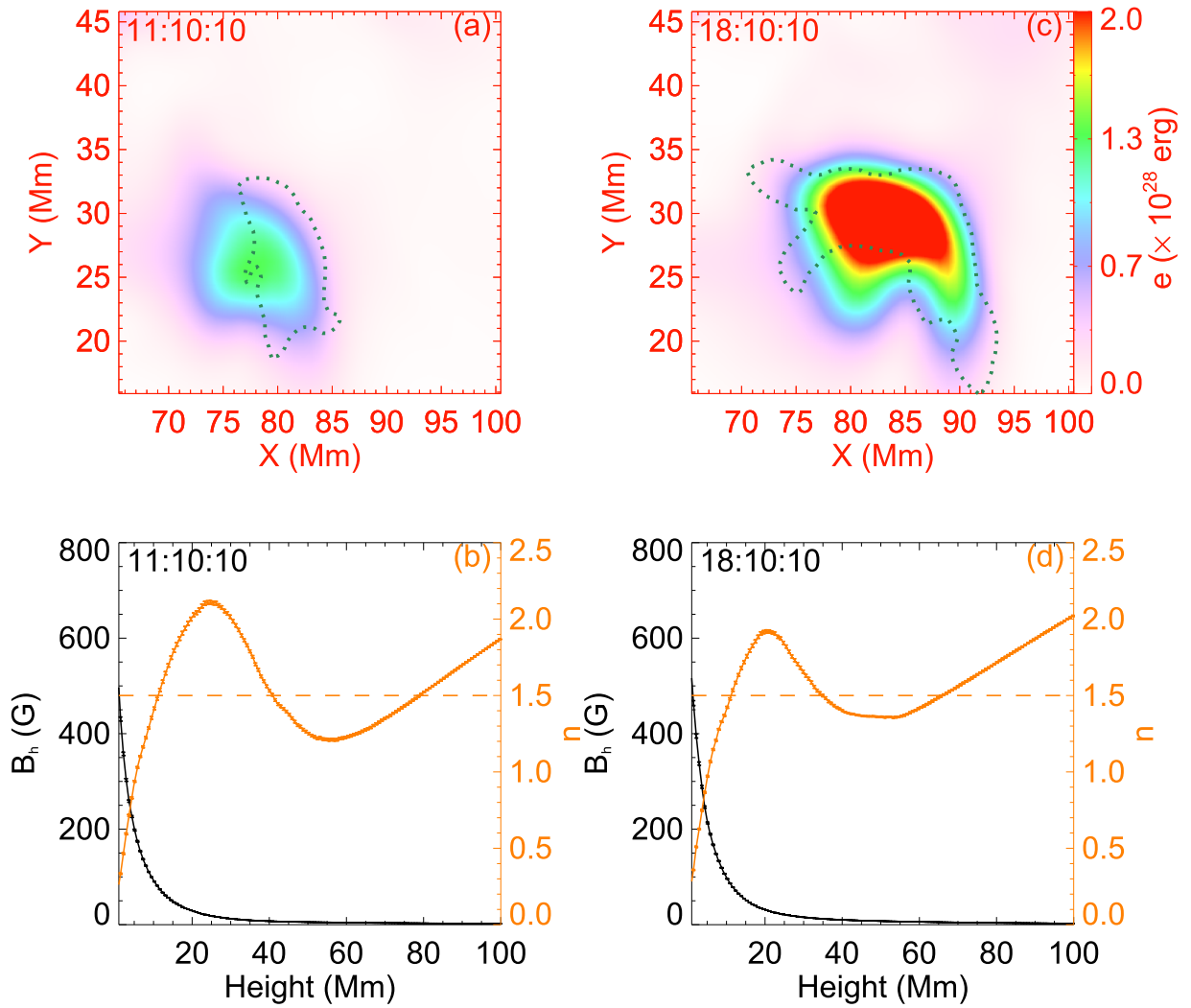
Figure 7. Coronal magnetic conditions shortly before the two eruptions: (a) and (b) for eruption1, and (c) and (d) for eruption2. (a) Pre-eruption1 magnetic free energy map with the same FOV as Figure 1(a). Each pixel represents the free energy integrated in a volume that takes the pixel at the photosphere, and the one at the height of 42 Mm as the lower and upper boundaries. The energy value saturated at $[0, 2.0 \times 10^{28}]$ erg. The dotted green lines outline the FPILs. (b) B_h and the decay index n distribution from 0 to 100 Mm are shown as the black and orange curves, respectively, with the standard error overplotted. Values at each height are the median values in the FPIL mask region. The position where n reaches the critical value 1.5 is outlined by the orange dashed line. (c) and (d) have the same layout as (a) and (b) but for the time instance before eruption2.

3.3. Eruption-related Change

A flux-rope-locating method, using the combination of the twist number and the squashing factor Q calculated from the reconstructed 3D coronal magnetic fields (Liu et al. 2016b), is performed to find the possible pre-existing flux rope. However, no coherent pre-existing flux rope can be located before both eruptions. Therefore, the result is not presented here. We then checked the detailed configuration of the magnetic fields above the source PIL in the extrapolated coronal fields before and after the eruptions. For eruption1, the result is shown in Figure 8 (panels (a) and (b)). Before the eruption, two sets of sheared field lines (SA1 and SA2 in Figure 8(a)) that corresponded well with the sheared arcades observed by AIA (see the background of Figure 8(a), or SA1 and SA2 in Figure 2(a)) were found. Note that the coronal magnetic fields are reconstructed using the HMI SHARP cutout magnetograms as photospheric boundaries, which limits the extrapolation cube region so that sometimes the extrapolated field lines may go in and out of the boundary, as the field lines of SA2 in Figure 8(a) showed: their southern part was out of the

extrapolation box. However, the northern part (left in the box) coincided well with the corresponding arcades observed by AIA (SA2 in Figure 2(a)). The extrapolated fields also met the divergence-free and force-free condition required by the NLFFF method (details are in the Appendix). Thus, we still take the result. After eruption1, the two sets of the sheared field lines cannot be identified, neither in the AIA observation (background of Figure 8(b)) nor in the reconstructed magnetic fields. On the contrary, near-potential loops can be identified in both the observation and the model coronae (cyan field lines marked as PFL in Figure 8(b)). Combined with the evolution of the eruption, we argue that a reconnection between the two sets of sheared arcades that formed the eruption core may have happened.

In addition to checking the topology change, we also checked the change of the photospheric B_h as shown in Figure 8(c). The map is projected into CCD coordinates to be compared with Figures 8(a) and (b). A clear enhancement of B_h was discernible in the FPIL region (outlined by a black curve in Figure 8(c)). The change of the Lorentz force, calculated by Equation (4), gave a
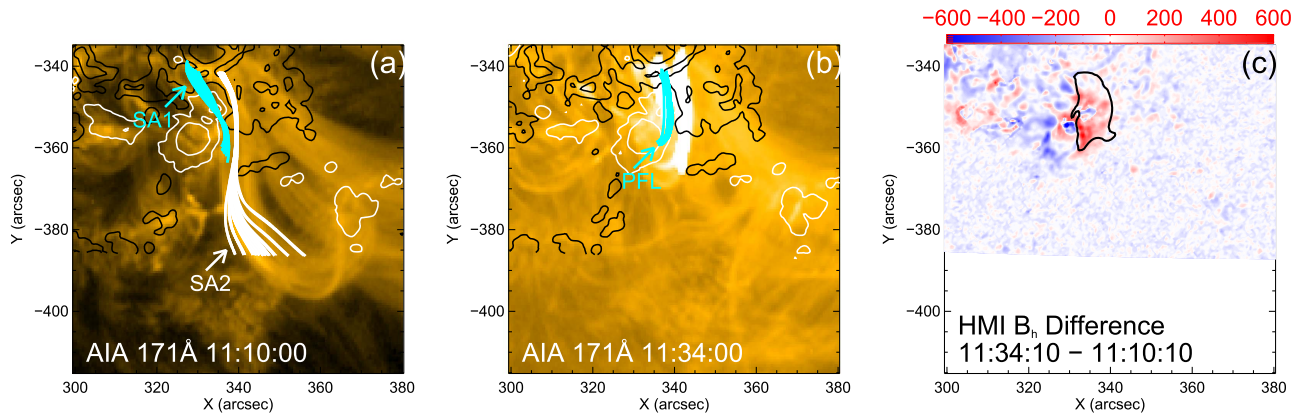
Figure 8. Eruption1-related change. (a) and (b) have the same FOV as Figures 2(a)–(b). SA1 (sheared arcade1) and SA2 in (a) are two sets of sheared field lines extracted from the reconstructed coronal magnetic fields based on the NLFFF method at the time instance before the eruption. The field lines are overplotted on the image taken by AIA 171 Å at the same time. The PFL in (b) refers to the post-eruption loops extracted from the model coronal fields after the eruption. The background of (b) is the observation in AIA 171 Å at the same time. The white/black contours in (a) and (b) outline the photospheric B_z at [800, 200, −200, −800] G. (c) shows the difference between the photospheric B_h before and after the eruption, which saturates at [−600, 600] G. The black curve outlines the FPIL for eruption1. The magnetogram in (c) is projected from the CEA heliographic coordinates to the CCD coordinates, with the same FOV as (a) and (b).
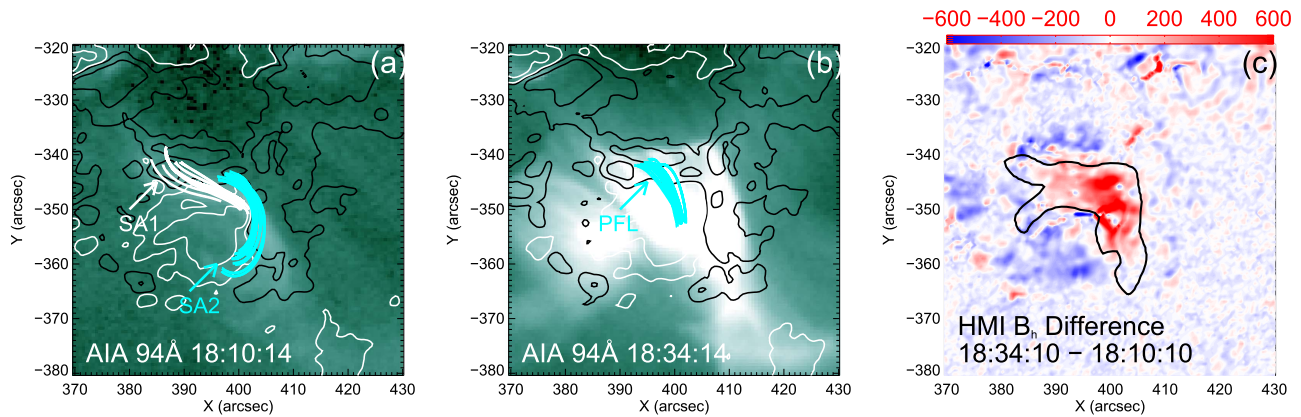

Figure 9. Eruption2-related change. The layouts are similar to those in Figure 2. The backgrounds of (a) and (b) are observations taken in AIA 94 Å.

value of 0.11×10^{22} dyn. Meanwhile, the magnetic free energy showed a decrease of 0.47×10^{31} erg (see Table 1).

For eruption2, similar changes are derived and shown in Figure 9. Before the eruption, two sets of sheared field lines (SA1 and SA2 in Figure 9(a)) above the PIL can be identified, which corresponded well with the position of the sheared arcades observed by AIA (backgrounds in Figure 9(a) and SA1, SA2 in Figure 4(a)). After eruption2, the two sets of the sheared field lines were not discernible anymore, and near-potential loops were found above the source PIL (exemplary loops are shown as PFL in Figure 9(b)). In addition to the topology change of the fields, the enhancement of the photospheric B_h in the FPIL can also be recognized (Figure 9(c)). The change of the Lorentz force had a value of 1.64×10^{22} dyne, which was an order of magnitude larger than the value of the force change in eruption1. The magnetic free energy also showed a larger decrease of 0.83×10^{31} erg (shown in Table 1).

In summary, the derived topology changes in the reconstructed magnetic fields support that for both eruptions a reconnection between the sheared arcades above the source PIL may have happened. Compared to the failed eruption, the successful eruption revealed a larger change in the Lorentz force and a stronger decrease in the magnetic free energy.

4. Summary and Discussion

4.1. Summary

In this work, we performed a detailed comparative study between a failed and a successful eruption that initiated from the same PIL within NOAA AR 11387 from perspectives of their eruption details, pre-eruption magnetic conditions, and eruption-related changes by stereoscopic observation from *SDO* and *STEREO-A*. The results are summarized as follows:

1. For the failed eruption (eruption1), two sets of sheared arcades above the source PIL can be identified from AIA observations before the eruption. The sheared arcades were likely to reconnect during the flare, and led to the formation of a flux-rope-like core structure that drove the outward eruption. The structure rose slowly with writhing motion and mass drainage, and finally stopped, and gradually became invisible afterward. The process fits into the scenario of a failed eruption of a helical kinked flux rope (e.g., Fan 2005; Guo et al. 2010; Török et al. 2010; Hassanin & Kliem 2016). The core structure had a peak velocity of 178 km s^{-1}, and ceased at a height around 0.24 R_{Sun}. For the successful eruption (eruption2), two sets of sheared arcades above the PIL were also identified before its onset. Their corresponding footpoints

brightened during the flare, indicating a reconnection between them. The eruption rapidly evolved into a fast CME (with a peak velocity of $1041 \, \mathrm{km \, s^{-1}}$) that propagated into the heliosphere.

2. Before both eruptions, continuous flux emergence existed in the source AR. For the source polarity pair, the positive one displayed a faster westward motion than the negative one, resulting in a net convergence toward the PIL. Due to continuous flux emergence and shear motion on the photosphere, magnetic helicity was injected, with a dominating shear term. A larger quantity of magnetic free energy and magnetic helicity was accumulated before the successful eruption. Before the onset of the eruptions, the core region, i.e., the source FPIL of the successful eruption, displayed a larger non-potentiality than the failed eruption. For example, before the successful eruption, more magnetic free energy resided above the FPIL, and larger values were derived for the mean current density, current helicity, and the shear angle that measures the core region's non-potentiality. The decay index distributions showed no significant difference, although the critical height for the successful eruption was slightly lower (around 3 Mm) than that for the failed eruption. The ratio of magnetic fluxes at 42 Mm and 2 Mm (in the FPIL mask) was smaller before the successful eruption, indicating a relatively weaker confinement.

3. Before the failed eruption, two sets of sheared field lines that corresponded well with the observed sheared arcades, could be identified in the coronal magnetic fields extrapolated by the NLFFF method. After the eruption, the sheared field lines disappeared, while near-potential loops were identified above the PIL. Combined with the observed eruption process, we conjecture that a reconnection between the sheared arcades may have occurred. A similar topology change was found during the successful eruption. Significant enhancements of B_h were found in the FPILs after both eruptions, while the value of the Lorentz force change during the successful eruption was an order of magnitude larger than that for the failed eruption. Decreases in magnetic free energy were also found after both eruptions, although the magnitude for the successful eruption was larger than that for the failed one.

4.2. Discussion

The associated flares of the two eruptions had different intensities, C8.4-class and M4.0-class, for the failed and the successful one, respectively. In general, the CME association rate increases when flare intensity increases, but the rate values for C8.4-class and M4.0-class are 45% and 65%, respectively (see Figure 1 in Yashiro et al. 2006), which are comparable. The event choice here is therefore adequate. During the failed eruption, an extremely faint corona outflow, without coherent shape or clear front, appeared in the FOV of COR1, soon diffused and failed to travel to a distance larger than $1 \, R_{\mathrm{Sun}}$. Observation of COR2 and LASCO (Brueckner et al. 1995) confirmed the absence of a successful CME. These kinds of literal "coronal mass ejections" that appeared in the inner corona but failed to propagate to a large distance, are defined as "pseudo-" or "failed-" CMEs in Vourlidas et al. (2010, 2013), which are thought to be different from the flux-rope-related CMEs, as they may not be magnetically driven. Therefore, we argue that defining eruption1

as a failed eruption is reasonable. The physical nature of this kind of "pseudo-" CME is worth further study.

Enhancement of B_h, which was observed during both eruptions, consists with the "magnetic implosion" scenario, in which the enhanced B_h is thought to be attributed to the contraction of the field loops due to the decrease of the magnetic pressure resulted by the eruption (e.g., Hudson 2000; Wang & Liu 2010; Liu et al. 2012; Wang et al. 2012a). When no eruption happens, the solar atmosphere is in a quasi-static, i.e., roughly force-free state. The state does not stand during the eruption. Using the change of the magnetic fields during the eruption, the change of the upward Lorentz force exerted on the ejecta can be calculated by Equation (4), of which the temporal integral will represent the Lorentz force impulse. A larger impulse results in a larger momentum of outward ejecta, indicating a faster velocity if the mass of the ejecta is comparable (Equation (14) in Fisher et al. 2012). For the above two eruptions, although the precise times during which the Lorentz force acting on the ejecta cannot be obtained, their associated flares have comparable durations, thus the Lorentz force impulses may be reflected directly by the changes of the force. During the successful eruption, an order of magnitude larger Lorentz force change was found, consisting with the result of Sun et al. (2015), in which the Lorentz force change in an X3.1-class confined flare from NOAA AR 12192 was smaller than that in other eruptive flares. Furthermore, the successful eruption had a larger peak velocity in the low corona than the failed eruption. We therefore argue that a large Lorentz force impulse, recorded by the Lorentz force change, may be important for a successful eruption, which will give the medium weight ejecta a large initial velocity, making it quickly enter the region with weak confinement and escape the Sun. The Lorentz force change, as an easily computed parameter, has been confirmed by Wang et al. (2012b) to be linearly correlated to the magnitudes of the flares. Its correlation to the eruptiveness of the flares is worth a further statistical study.

It should be noted that the Lorentz force change (or force impulse) may not be a sufficiently independent parameter. Considering the original form of the equation for Lorentz force: $F = \int_V J \times B \, dV$, a non-zero force first requires the existence of current in the volume, which is related to the non-potentiality of the magnetic fields; it second requires the current density to have a component perpendicular to the magnetic field lines, i.e., it is additionally influenced by the field configuration. In addition, the force change can only be obtained after the eruption, which may not be practical to pre-evaluate the potential of a source region for producing CMEs. However, it still reflects the property of the force acting on the ejecta during the eruption, which may also be important as the pre-eruption conditions of the source region for determining the final state of the ejecta.

Before both eruptions, the decay index distribution displayed a "saddle-like" profile, exhibiting a local torus-stable ($n < 1.5$) region higher than the critical height, enclosed by two torus-unstable domains. This kind of profile is found to be exclusive in ARs with multipolar configurations, and may provide extra confinement when the erupting core structure enters this torus-stable region without a well-developed disturbance (Wang et al. 2017). In our failed eruption, the erupting core reached a height around $0.24 \, R_{\mathrm{Sun}}$, which was higher than the critical height or the local torus-stable region. It rose quickly in the lower torus-unstable region, but slowed down largely after passing through the torus-stable region. It exhibited a writing

motion that converted the twist to the writhe of the structure axis, which is a typical behavior in the course of helical kink instability, suggesting a flux rope configuration of itself, and a possible "self-consistent" reformation. It may have regained an equilibrium state due to the stronger confinement in the torus-stable region, rose more slowly and finally halted. For the successful eruption, the erupting structure had larger energy/initial velocity to pass through the torus-stable region rapidly, and was kept in a non-equilibrium state with enough disturbance to erupt out. The local torus-stable region in our case, which is also found in some other failed eruptions (e.g., Guo et al. 2010; Wang et al. 2017), may play an important role in confining the eruption, especially those ones with small initial momentum. The result suggests that the role of the decay index in determining a full eruption should be considered by its entire distribution, rather than a single critical height.

Before both eruptions, no pre-existing coherent flux rope can be found. However, sheared arcades were found above the PIL, which may have reconnected and initiated the eruptions. This is consistent with the result in Liu et al. (2016a), who concluded that pre-existing flux ropes or sheared structures are necessary conditions for successful CMEs, although not sufficient ones.

In summary, we analyzed two eruptions initiated from the same PIL, one with a failed erupted core and a faint inner corona outflow that is defined as a failed eruption, and one with a fully evolved CME that is defined as a successful eruption. They both started from reconnection between different sets of sheared arcades above the source PIL due to converging motion, during which the flux ropes may have formed and driven the eruptions. The successful eruption had a larger velocity than the failed one. Although originating from the same PIL, they had distinct pre-eruption magnetic conditions: for the successful eruption, the source region underwent a more severe shear motion, and accumulated more helicity and free energy, leading to a core region with a larger non-potentiality before the eruption started; the external magnetic fields displayed a similar decay index distribution (a "saddle-like" profile) but smaller flux ratio

(between values in the planes at 42 Mm and 2 Mm) compared to the conditions for the failed eruption. The Lorentz force change exerted on the outward ejecta over the course of the eruption, which can represent the force impulse, was an order of magnitude larger than that for the failed eruption. We argue that the weaker non-potentiality in the core region, smaller Lorentz force impulse during the eruption, and the local torus-stable region in the coronal magnetic fields are together responsible for the failed eruption: the core structure erupted with a small momentum due to weaker non-potentiality in its source and a small Lorentz force impulse exerted on it, may have regained an equilibrium state due to the strong confinement in the torus-stable region, and thus failed to fully erupt. The Lorentz force impulse during the eruption (which may be related to the non-potentiality and the configuration of the source fields), and the local torus-stable regions in the corona may play important roles in initiating and confining the eruptions.

Appendix
Quality of the NLFFF Extrapolation

In this study, we reconstruct the coronal magnetic fields based on an NLFF assumption, which requires the model fields to meet the force-free and divergence-free condition. Following
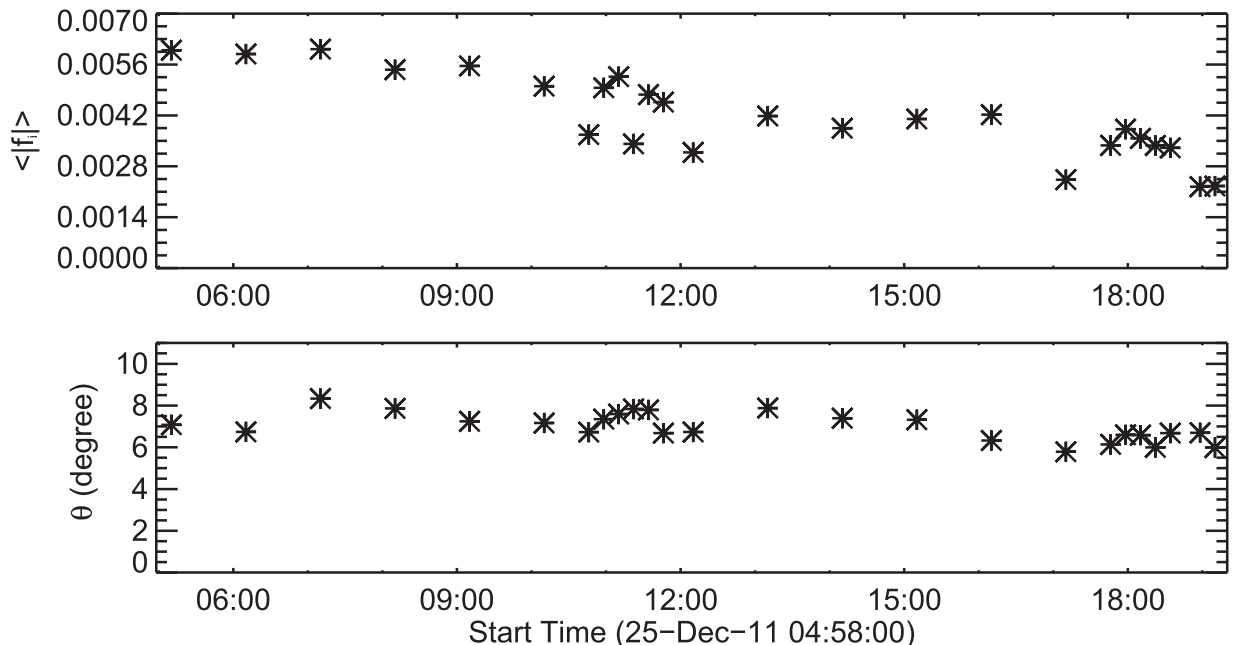

Figure 10. Divergence-free and force-free parameters for the model fields in the context. The figure has the same time axis as Figure 6 (c). The upper panel displays the values of the divergence-free parameter $\langle |f_i| \rangle$. The lower panel shows the values of the force-free parameter θ.

Wheatland et al. (2000) and Liu et al. (2016b, 2017), we calculate two parameters: the fractional flux increase ($\langle|f_i|\rangle$) and the angle between the fields and the current density (θ) in the extrapolated volume to check their qualities. The computing equations are as follows:

$$\langle|f_i|\rangle = \frac{1}{n}\sum_{i=1}^{n}\frac{|\nabla\cdot\boldsymbol{B}|_i\,\Delta V_i}{B_i\cdot\Delta S_i}$$

$$\theta = \sin^{-1}\left(\left(\sum_{i=1}^{n}\frac{|\boldsymbol{J}\times\boldsymbol{B}|_i}{B_i}\right)\bigg/\sum_{i=1}^{n}J_i\right).$$

n denotes the number of the cells in the calculation volume, $\boldsymbol{B}$ refers to the magnetic fields, $\boldsymbol{J}$ denotes the current density, the subscript "i" refers to the i_{th} cell, and ΔV and ΔS refer to the volume and the surface area of each cell. See Figure 10 for the qualities of the model fields in context. $\langle|f_i|\rangle$ are all well below 0.007, while θ are all well below $10°$, confirming that the model fields all meet the force-free and divergence-free condition.

ORCID iDs

Lijuan Liu ⓞ https://orcid.org/0000-0001-6804-848X
Yuming Wang ⓞ https://orcid.org/0000-0002-8887-3919
Zhenjun Zhou ⓞ https://orcid.org/0000-0001-7276-3208
Karin Dissauer ⓞ https://orcid.org/0000-0001-5661-9759
Manuela Temmer ⓞ https://orcid.org/0000-0003-4867-7558
Jun Cui ⓞ https://orcid.org/0000-0002-4721-8184

References

Alexander, D., Liu, R., & Gilbert, H. R. 2006, ApJ, 653, 719
Amari, T., Luciani, J. F., Mikic, Z., & Linker, J. 1999, ApJL, 518, L57
Amari, T., Luciani, J. F., Mikic, Z., & Linker, J. 2000, ApJL, 529, L49
Bein, B. M., Berkebile-Stoiser, S., Veronig, A. M., et al. 2011, ApJ, 738, 191
Bein, B. M., Berkebile-Stoiser, S., Veronig, A. M., Temmer, M., & Vršnak, B. 2012, ApJ, 755, 44
Berger, M. A. 1984, GApFD, 30, 79
Bobra, M. G., Sun, X., Hoeksema, J. T., et al. 2014, SoPh, 289, 3549
Brueckner, G. E., Howard, R. a., Koomen, M. J., et al. 1995, SoPh, 162, 357
Canfield, R. C., Hudson, H. S., & McKenzie, D. E. 1999, GeoRL, 26, 627
Chandra, R., Schmieder, B., Mandrini, C. H., et al. 2011, SoPh, 269, 83
Chen, H., Zhang, J., Ma, S., et al. 2015, ApJL, 808, L24
Cheng, X., Zhang, J., Ding, M. D., Guo, Y., & Su, J. T. 2011, ApJ, 732, 87
DeVore, C. R., & Antiochos, S. K. 2008, ApJ, 680, 740
Falconer, D. A., Moore, R. L., & Gary, G. A. 2002, ApJ, 569, 1016
Falconer, D. A., Moore, R. L., & Gary, G. A. 2006, ApJ, 644, 1258
Fan, Y. 2005, ApJ, 630, 543
Fan, Y. 2010, ApJ, 719, 728
Fisher, G. H., Bercik, D. J., Welsch, B. T., & Hudson, H. S. 2012, SoPh, 277, 59

Guo, Y., Ding, M. D., Schmieder, B., et al. 2010, ApJL, 725, L38
Harrison, R. A. 1995, A&A, 304, 585
Hassanin, A., & Kliem, B. 2016, ApJ, 832, 106
Hoeksema, J. T., Liu, Y., Hayashi, K., et al. 2014, SoPh, 289, 3483
Howard, R. A., Moses, J. D., Vourlidas, A., et al. 2008, SSRv, 136, 67
Hudson, H. S. 2000, ApJL, 531, L75
Ji, H., Wang, H., Schmahl, E. J., Moon, Y.-J., & Jiang, Y. 2003, ApJL, 595, L135
Kaiser, M. L., Kucera, T. a., Davila, J. M., et al. 2008, SSRv, 136, 5
Kliem, B., & Török, T. 2006, PhRvL, 96, 255002
Kumar, P., Cho, K.-S., Bong, S.-C., Park, S.-H., & Kim, Y. H. 2012, ApJ, 746, 67
Lemen, J. R., Title, A. M., Akin, D. J., et al. 2012, SoPh, 275, 17
Lin, J., & Forbes, T. G. 2000, JGR, 105, 2375
Liu, C., Deng, N., Liu, R., et al. 2012, ApJL, 745, L4
Liu, L., Wang, Y., Liu, R., et al. 2017, ApJ, 844, 141
Liu, L., Wang, Y., Wang, J., et al. 2016a, ApJ, 826, 119
Liu, R., Kliem, B., Titov, V. S., et al. 2016b, ApJ, 818, 148
Liu, Y. 2008, ApJL, 679, L151
Liu, Y., Hoeksema, J. T., Bobra, M., et al. 2014, ApJ, 785, 13
Liu, Y., & Schuck, P. W. 2012, ApJ, 761, 105
Liu, Y., Su, J., Xu, Z., et al. 2009, ApJL, 696, L70
Nindos, A., & Andrews, M. D. 2004, ApJL, 616, L175
Pesnell, W. D., Thompson, B. J., & Chamberlin, P. C. 2012, SoPh, 275, 3
Petrie, G. J. D. 2012, ApJ, 759, 50
Petrie, G. J. D. 2013, SoPh, 287, 415
Roussev, I. I., Forbes, T. G., Gombosi, T. I., et al. 2003, ApJL, 588, L45
Sakurai, T. 1989, SSRv, 51, 11
Schmieder, B., Démoulin, P., & Aulanier, G. 2013, AdSpR, 51, 1967
Schuck, P. W. 2008, ApJ, 683, 1134
Shen, Y.-D., Liu, Y., & Liu, R. 2011, RAA, 11, 594
Sun, X., Bobra, M. G., Hoeksema, J. T., et al. 2015, ApJL, 804, L28
Thalmann, J. K., Su, Y., Temmer, M., & Veronig, a. M. 2015, ApJL, 801, L23
Thalmann, J. K., Wiegelmann, T., & Raouafi, N.-E. 2008, A&A, 488, L71
Thompson, W. T., Davila, J. M., Fisher, R. R., et al. 2003, Proc. SPIE, 4853, 1
Török, T., Berger, M. A., & Kliem, B. 2010, A&A, 516, A49
Török, T., & Kliem, B. 2005, ApJL, 630, L97
Vemareddy, P. 2017, ApJ, 845, 59
Vourlidas, A., Howard, R. A., Esfandiari, E., et al. 2010, ApJ, 722, 1522
Vourlidas, A., Lynch, B. J., Howard, R. A., & Li, Y. 2013, SoPh, 284, 179
Wang, D., Liu, R., Wang, Y., et al. 2017, ApJL, 843, L9
Wang, H., & Liu, C. 2010, ApJL, 716, L195
Wang, H., & Liu, C. 2015, RAA, 15, 145
Wang, S., Liu, C., Liu, R., et al. 2012a, ApJL, 745, L17
Wang, S., Liu, C., & Wang, H. 2012b, ApJL, 757, L5
Wang, Y., Liu, L., Shen, C., et al. 2013, ApJL, 763, L43
Wang, Y., & Zhang, J. 2007, ApJ, 665, 1428
Wheatland, M. S., Sturrock, P. a., & Roumeliotis, G. 2000, ApJ, 540, 1150
Wiegelmann, T. 2004, SoPh, 219, 87
Wiegelmann, T., Inhester, B., & Sakurai, T. 2006, SoPh, 233, 215
Wiegelmann, T., Thalmann, J. K., Inhester, B., et al. 2012, SoPh, 281, 37
Wuelser, J.-P., Lemen, J. R., Tarbell, T. D., et al. 2004, Proc. SPIE, 5171, 111
Yashiro, S., Akiyama, S., Gopalswamy, N., & Howard, R. a. 2006, ApJL, 650, L143
Zhang, J., Cheng, X., & Ding, M.-D. 2012, NatCo, 3, 747
Zhang, J., & Wang, J. 2002, ApJL, 566, L117